



# Effects of base plate temperature on microstructure evolution and high-temperature mechanical properties of IN718 processed by laser powder bed fusion using simulation and experiment

Koji Kakehi<sup>1</sup> · Hasina Tabassum Chowdhury<sup>1</sup> · Yusuke Shinoda<sup>1</sup> · Palleda Thaviti Naidu<sup>1</sup> · Naoto Kakuta<sup>1</sup> · Shohei Ishisako<sup>2</sup>

Received: 26 July 2023 / Accepted: 11 January 2024 / Published online: 27 January 2024  
© The Author(s) 2024

## Abstract

Base plate preheating is a relatively new strategy to influence the mechanical properties and microstructure of IN718. Base plate preheating was studied to reduce Niobium (Nb) segregation in the interdendritic region of IN718 superalloy and to improve mechanical properties through the laser powder bed fusion (L-PBF) process. Here, we compared experimental results for high-temperature (650°C) mechanical properties of specimens built with 200°C (PH200) and 600°C (PH600) preheated base plates. The as-built PH200 and PH600 specimens had relatively similar grain morphologies and orientations along the building direction. The PH200 specimen showed a cellular structure and higher Nb segregation at the interdendritic region, whereas the PH600 specimen had a dendritic structure and lower Nb segregation. The lower amount of Nb segregation in the PH600 specimen is mainly because of the cooling rate difference between specimens during the L-PBF process. The PH600 specimen exhibited slightly better tensile properties, longer creep life, and elongation than the PH200 specimen in both the as-built and heat-treated conditions. These differences mainly occurred due to differences in Laves and  $\delta$ -phase fractions between the PH200 and PH600 specimens. The simulation result indicates that the temperature distribution in the block remains relatively uniform during the building process.

**Keywords** Laser powder bed fusion · selective laser melting · Base plate preheating · Inconel 718 · Tensile strength · Creep · Nb segregation

## 1 Introduction

Rapid prototyping is one of the primary additive manufacturing (AM) processes. This enables the formation of printed parts, not just models. Important advances in product development resulting from this process include reductions in time, cost, and human interaction, hence shortening the product development cycle [1–6]. AM is defined as the process of combining materials to create objects from 3D

model data, usually layer by layer, and can deliver highly complex and intricately shaped parts while minimizing the need for post-processing with almost zero material waste [7, 8]. This increases design freedom and enables engineers and designers to create unique products that can be economically manufactured in small quantities [9–12]. The two main processes use powder as a raw material to make the 3D products [13–15]. Most systems use laser power to melt metal material in a process called laser powder bed fusion (L-PBF). In this process, the powder is melted to form a part. The laser beam power is normally high (around 400 W). After each layer is made, the bed is lowered, and a new layer of powder is applied. After that, the rotating roller is used to evenly spread the powder. While the unsintered material powder supports the structure, the melted material forms the part [16, 17]. The unsintered material can be cleaned and recycled after the building is completed [18–20]. However, this process causes the problem of non-uniform thermal field distribution, resulting in thermal distortion and cracks on the

✉ Koji Kakehi  
kkakehi@tmu.ac.jp

✉ Hasina Tabassum Chowdhury  
tabassum.u@duet.ac.bd

<sup>1</sup> Department of Mechanical Systems Engineering,  
Tokyo Metropolitan University, 6-6 Asahigaoka,  
Hino-city, Tokyo 191-00657, Japan

<sup>2</sup> Aichi Sangyo CO., LTD, Shinagawa-ku, Japan

product [21]. Despite the many privileges of L-PBF (such as high accuracy and surface quality), the process still faces many challenges which need to be addressed before widespread application. Randomly dispersed defects and microstructure heterogeneities are two of the main challenges. These also deteriorate the mechanical properties [22]. Much research effort has been devoted to optimize the processing parameters [22, 23], building orientation [24, 25], scanning strategy [26], and base plate preheating to obtain final parts with high density and optimal mechanical properties. Centrosymmetric joint path strategy is the optimal laser path (preheated temperature during building was 100°C) [27] and can maximize the absorption capacity of energy for a Taylor bar structure [28]. Optimal material distribution can be obtained by improved evolutionary structural optimization method for Taylor bar [29]. Base plate preheating is a vital variable that affects the thermal history during the L-PBF process and thus put an effect on the specimen density, residual stresses [30], and evolution of the microstructures, eventually changing a part's mechanical properties [31]. However, few researchers have assessed the effects of base plate preheating on creep properties and other mechanical properties.

Nickel-based superalloys have excellent properties, such as toughness, strength, and corrosion resistance at high temperatures [32–34]. Inconel 718 also has good structural stability and weldability at temperatures up to 650°C like other superalloys [35]. Thus, the IN718 superalloy has been widely used in gas turbine disks, aircraft engines, and nuclear reactors [36, 37]. However, conventional casting techniques offer limited component complexity. The ability to produce geometries of high complexity is needed to reduce component weight and material consumption [38, 39]. Almost all the research strategies involve changing the microstructure of AM materials for better mechanical properties to satisfy industrial needs. Significantly, the segregation of Nb at the interdendritic region leads to the formation of Laves phase [40]. It will also result in the formation of the  $\delta$ -phase after heat treatment which causes inferior mechanical properties due to its embrittlement nature with the  $\gamma$ -matrix [41]. So, controlling Nb segregation at interdendritic regions is essential during the L-PBF process. Heating by laser irradiation and cooling by argon gas flow, the latter of which removes fumes, are repeated on the built specimen. Very large temperature fluctuations, such as fluctuations in temperature amplitude and cooling rate on the order of 10<sup>6</sup>°C/s, occur during thermal cycles of L-PBF [42]. One way to reduce

Nb segregation at interdendritic areas is to lower the cooling rate of molten liquid during L-PBF. This could be done by keeping the base plate at certain temperatures to reduce the thermal gradient. Very few studies have assessed the effects of base plate preheating on the microstructures and mechanical properties of IN718 Ni-based superalloy processed by L-PBF. Park et al. compared three different preheated temperatures (50°C, 100°C, and 150°C) on the mechanical properties of Inconel 718 built with selective laser manufacturing process and found that with the increase of the preheating temperatures, the residual stress is decreasing [43]. Average Vickers hardness increases and porosity decreases along with the increasing of the preheating temperature [43]. According to Chen et al., melt pool depth and length increase significantly with higher preheating temperatures (test temperatures: 100°C, 200°C, 300°C, 400°C, and 500°C) [44]. These results motivated us to know more detail about thermal properties built with preheated base plate.

So, in this study, we used base plate preheating and built two kinds of IN718 superalloy blocks using L-PBF (selective laser melting process) in an argon atmosphere. One kind was built by base plate preheating at 200°C, and the other at 600°C. By preheating the base plate, the material's thermal gradient would decrease, which would reduce the segregation of elements, especially Nb, in the as-built specimen and influence the mechanical properties. We want to know the temperature distribution for the built block when using the preheated base plate. However, measuring the surface temperature of the built block inside the machine is difficult. So, we use simulation to know the temperature distribution during the process.

Thus, this study aimed to assess the effects of base plate preheating on the microstructures and high temperature mechanical properties (tensile and creep) of IN718 built by the selective laser melting (SLM) process.

## 2 Materials and methods

### 2.1 Experimental setup

The chemical compositions (in mass%) of IN718 alloys are shown in Table 1.

45 × 45 × 45 mm cubes were built using the SLM 280HL with a preheating system (SLM Solutions Group AG, Estlandring, Lubeck, Germany) in a protective Ar atmosphere with the same processing parameters. Base plates were heated at

**Table 1** Chemical composition of IN718 powder used in SLM (mass %)

Ni	Cr	Nb	Mo	Ti	Al	Co	Cu	C	Mn	P	Fe
52.75	19.02	5.22	3.1	0.95	0.47	0.2	<0.2	0.06	0.04	0.006	18.07

**Table 2** Process parameters used to build PH200 and PH600 blocks

Power (W)	Scanning speed (mm/s)	Hatch spacing (μm)	Thickness (μm)
255	980	120	30

200°C and 600°C, and the specimens built on the preheated plates are called PH200 and PH600, respectively.

The processing parameters are listed in Table 2.

Standard heat treatment was conducted for both specimens. The heat treatment protocol begins with a solution heat treatment at 980°C for 1 h, followed by air cooling to room temperature and then a two-step aging treatment: first, the specimens are held at 718°C for 8 h, then furnace-cooled to 621°C; second, the specimens are held at 621°C for 10 h, then air-cooled to room temperature. The heat-treated specimens are called STA specimens hereafter.

For the tensile and creep tests, we sliced the cube into several slabs, each with a thickness of 3.1 mm; from these slabs, both test specimens were cut out using an electro-discharge wire cutting machine. The gauge dimensions of each specimen were 19.6 × 2.8 × 3.0 mm [45]. We conducted the tensile test at the high temperature (650°C) and the creep test under 650°C/550 MPa. For the microstructural observations, the specimens were polished using SiC emery paper up to grade 1200# followed by diamond paste up to colloidal silica (0.5 μm) using a Struers (Ballerup, Denmark) automatic polishing machine. All the specimens were then washed with ethanol in an ultrasonic bath for 10 min. We etched the specimens with 20% phosphoric acid + 80% water solution to observe the molten pool boundaries. The microstructural observation was conducted using an optical microscope (OM; Olympus, Tokyo, Japan), a scanning electron microscope (SEM; Hitachi, Tokyo, Japan), an energy-dispersive spectroscope (EDS) (S-3700N–type EDS equipment manufactured by Horiba Seisakusho, Kyoto, Japan), observation of electron backscatter diffraction (EBSD) images (Oxford Instruments, Oxfordshire, UK) used an accelerating voltage of 15 kV, and a scanning transmission electron microscope (STEM; JEOL, Tokyo, Japan). ImageJ image processing software (64-bit Java 1.8.0\_172) was used to measure Niobium (Nb) segregation and δ-phase fraction at the interdendritic region and porosity in the SLMed material.

## 2.2 Simulation

To evaluate the effect of preheating the base plate on the temperature distribution of IN718, we also simulated it with COMSOL Multiphysics software (version 6.1).

The temperature-dependent properties (density, heat capacity, and heat conductivity) of IN718 are used as the

reference [46]. We considered the argon gas flow environment and laser irradiation during the simulation.

The equation for heat transfer in solids:

$$\rho C_p \frac{\partial T}{\partial t} = \nabla \cdot (k \nabla T) + Q_{laser} \tag{1}$$

where  $\rho$  is the density [kgm<sup>-3</sup>],  $C_p$  is the specific heat [Jkg<sup>-1</sup>K<sup>-1</sup>],  $T$  is the temperature [K],  $t$  is time [s],  $k$  is the thermal conductivity [Wm<sup>-1</sup>K<sup>-1</sup>], and  $Q_{laser}$  is the laser heat source [Wm<sup>-3</sup>].

On the powder surface, the convective and radiative heat transfer occurs:

$$k \frac{\partial T}{\partial z} \Big|_{z=0} = h(T_{ext} - T) + \epsilon \sigma (T_{amb}^4 - T^4) \tag{2}$$

where  $h$  heat transfer coefficient [Wm<sup>-2</sup>K<sup>-1</sup>],  $T_{ext}$  external gas temperature [K],  $\epsilon$  is the surface emissivity (a dimensionless number between 0 and 1),  $\sigma$  is the Stefan-Boltzmann constant,  $T_{amb}$  is the ambient radiant temperature [K], and  $z$  is z-direction depth within powder [m].

Assuming that the laser beam is a Gaussian beam, we used the Beer-Lambert law to define  $Q_{laser}$  [47]:

$$Q_{laser} = \frac{2p_{laser} A_{coeff}}{\pi r_{spot}^2 d} \exp \left\{ \frac{-2[(x-x_{laser})^2 + (y-y_{laser})^2]}{r_{spot}^2} \right\} \exp \left( \frac{-|z|}{d} \right) \tag{3}$$

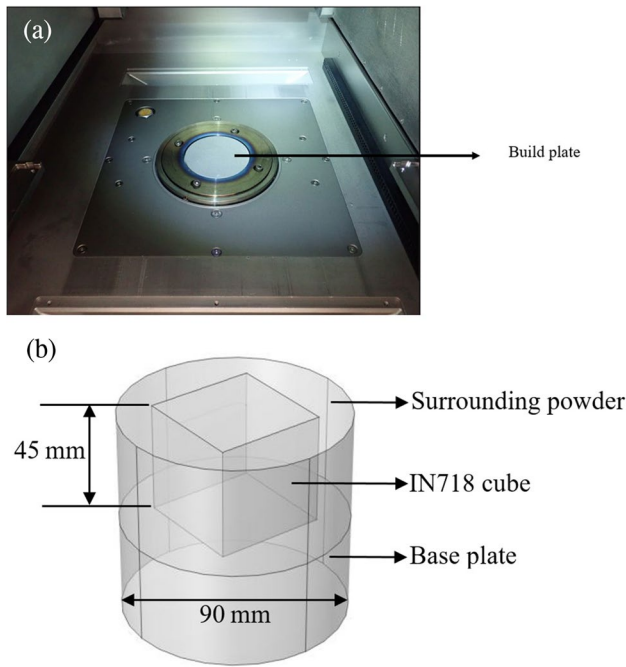
Here,  $p_{laser}$  is laser power [W],  $r_{spot}$  is beam radius [m],  $A_{coeff}$  is absorption coefficient,  $d$  is penetration depth [m], and  $x_{laser}$  and  $y_{laser}$  functions for laser positions during scanning.

The parameters used in this simulation are listed in Table 3.

Time-dependent solver has been used during the simulation. The preheated build plate setup photo from the

**Table 3** Parameters for simulation

Laser power, $p_{laser}$	255 W
Scanning speed	980 mm/s
Hatch spacing	120 μm
Base plate height	40 mm
Base plate radius	45 mm
Cube dimension	45 × 45 × 45 mm
Laser beam radius	80 μm
Absorption coefficient	0.3
Penetration depth	65 μm
Argon gas flow velocity	23 m/s
Cooling temperature of argon gas	45 °C
Emissivity	0.36
Heat transfer coefficient	80 Wm <sup>-2</sup> K <sup>-1</sup>
Melting temperature	1571 K
Solidus temperature	1443 K
Liquidus temperature	1609 K
Latent heat of fusion	210 J/g
Preheated temperatures	200 °C, 600 °C



**Fig. 1** a Preheated build plate setup b Base plate with IN718 cube

experiment is included in Fig. 1a. The steel base plate is preheated and the IN718 cube is surrounded by unsintered powder (Fig. 1b).

The simulation runs for 60 min. The initial and boundary conditions are as follows in Table 4:

### 3 Results

#### 3.1 Temperature distribution of IN718 cube during the additive manufacturing process

The simulation study was for 60 min. The following figures show the surface temperature and center plane temperature for preheated base plates 200°C (Fig. 2a) and 600°C (Fig. 2b).

According to these figures (Fig. 2a, b); when the base plate is preheated to 200°C, the temperature at the top surface

of the cube is 169°C while it is 517°C for the preheated 600°C base plate. This indicates the temperature changes were not large from the base plate to the top surface of the cube, i.e., the temperature distribution in the block is relatively uniform during the building process because both the build block and surrounding power are preheated. This means that during the build, the preheated base plate transfers heat to the cube and surrounding power.

We can observe the temperature at different locations of the cube. Figures 3 and 4 show the front view (*yz*-plane) and top view (*xy*-plane) of the model for the temperature distribution in thermal equilibrium.

The temperature of the cube becomes almost stable at about 169°C (base plate preheated 200°C) and about 517°C (base plate preheated 600°C) at the final process in thermal equilibrium.

The IN718 cube has different temperatures along the height with very little difference. In Fig. 5, the cube is above the base plate; so this point is 0 mm, and the height of the cube is 45 mm. For the preheated base plate of 200°C, point 0 mm has 200°C temperature and the top surface 45 mm has 169.28°C temperature, whereas these values are 600°C and 516.96°C respectively for preheated 600°C base plate.

### 3.2 Microstructure observation

#### 3.2.1 As-built condition

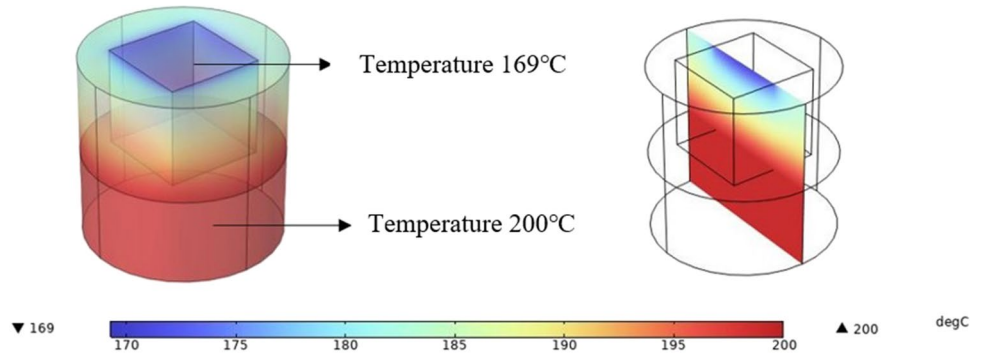
The microstructures of the as-built specimens of PH200 and PH600 are shown in Fig. 6. Both figures show molten pool boundaries formed due to laser beam tracking during SLM. Relatively few residual porosities were observed in both specimens.

Fine dendrites were identified in the molten pools in the PH200 and PH600 specimens. Various orientations tended toward the top center of the molten pool along the building direction (Fig. 7a, b). The PH200 specimen had a fine dendritic structure (Fig. 7a). The PH600 specimen had a coarser dendritic structure (Fig. 7b). The primary dendrite arm spacing ( $\lambda$ ) in the PH200 (Fig. 7a) and PH600 (Fig. 7b) specimens were

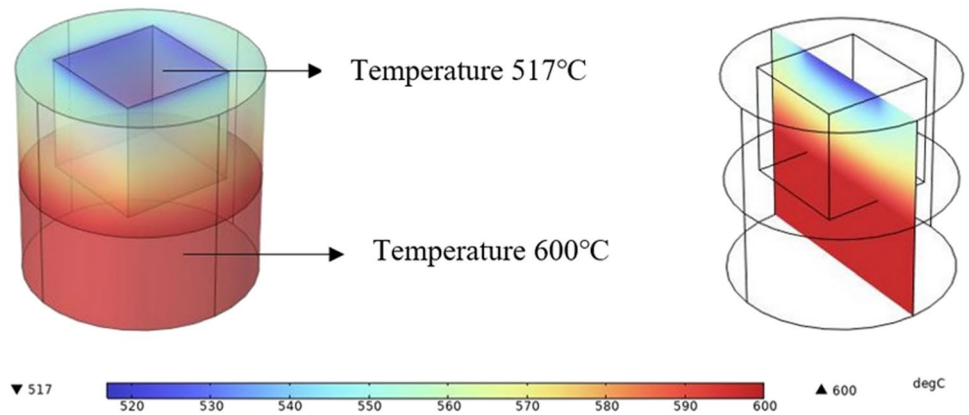
**Table 4** Initial and boundary conditions for simulation

Initial conditions	Boundary conditions	
IN718 cube → Room temperature (25 °C)	Top surface of IN718 cube →	Convection (convective heat transfer coefficient and using heat flux node)
Base plate → Preheated temperature (200 °C, 600 °C)		Argon cooling effect (external forced convection and using heat flux node)
Surrounded unsintered powder → 100 °C		Radiation (using Surface to ambient radiation node)
	Bottom surface of IN718 cube → Preheated temperature (200 °C, 600 °C) (using Temperature node)	

**Fig. 2** Temperature at the surface and center plane of the cube

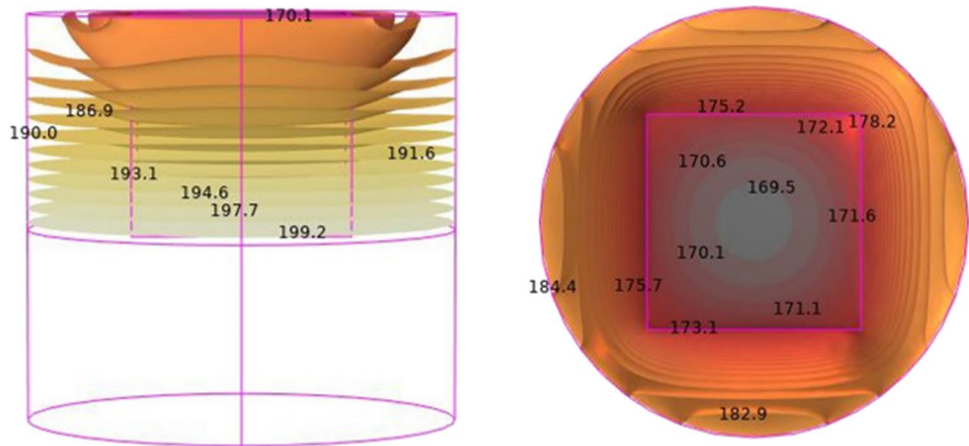


(a) base plate preheated at 200°C



(b) base plate preheated at 600°C

**Fig. 3** Temperature at different locations of the cube (base plate preheated 200°C) in thermal equilibrium



(a) yz-plane

(b) xy-plane

calculated by taking the average of 10 dendrites (10 PDAS) at different locations of the specimens by using Eq. 4 [48, 49].

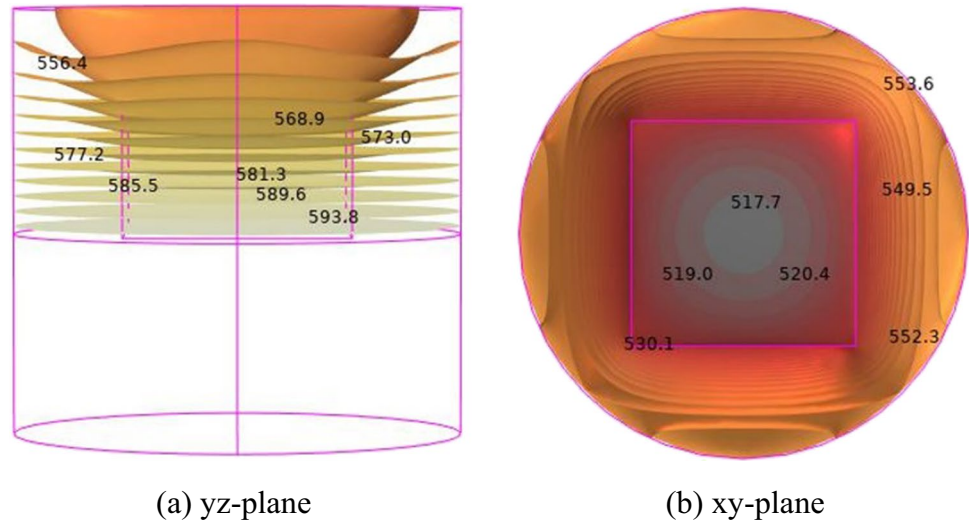
$$PDAS(\lambda) = 97(\dot{T})^{-0.36} \tag{4}$$

where

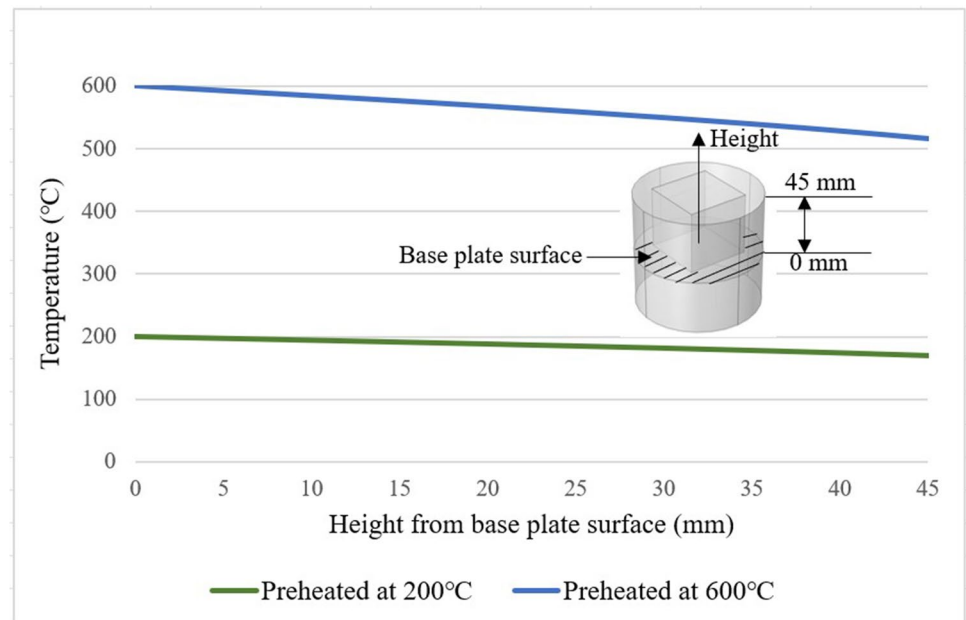
$\lambda$  Primary dendritic arm spacing (PDAS) ( $\mu\text{m}$ )  
 $\dot{T}$  Cooling rate ( $^{\circ}\text{C}/\text{sec}$ )

Table 5 shows the results of  $\lambda$  values in the averages and cooling rates ( $^{\circ}\text{C}/\text{sec}$ ). The PH200 as-built specimen exhibited the  $\lambda$  values of an average of 0.6  $\mu\text{m}$  to 0.7  $\mu\text{m}$ ,

**Fig. 4** Temperature at different locations of the cube (base plate preheated 600°C) in thermal equilibrium



**Fig. 5** Temperature distribution along the vertical center line of cube at the final process in thermal equilibrium



resulting in higher cooling rates. On the other hand, the PH600 as-built specimen presents  $\lambda$  values of an average of 0.9  $\mu\text{m}$  to 1.0  $\mu\text{m}$ , which causes a lower cooling rate during SLM compared to the PH200 as-built specimen. The cooling rates calculated from the dendritic arm spacing were equivalent (Table 5) because the temperatures did not change significantly in the block specimens (Fig. 5).

To clarify the segregation of the Nb element at the interdendritic region of both the PH200 and PH600 as-built specimens, STEM-EDS analysis was carried out, and the results are shown in Fig. 8.

In the PH200 specimen (Fig. 8a), the segregation of the Nb element at the interdendritic region is higher than that of the PH600 as-built specimen (Fig. 8b). In addition, we

measured the area fraction of Nb segregation in the PH200 and PH600 as-built specimens by using ImageJ software. The results are the averages of five different areas of both specimens. The Nb-rich area fractions were 5.94% in the PH200 as-built specimen and 0.84% in the PH600 specimen (Fig. 9). The Nb segregation in the PH200 specimen was found to be remarkable, whereas that of the PH600 specimen was not.

Figure 10 shows the as-built specimens' EBSD maps and grain aspect ratios (GARs). The vertical direction is parallel to the building direction. The PH200 and PH600 specimens both had a mixed-grain texture, including columnar grains and fine grains (Fig. 10a, b respectively). The columnar grains resulted from epitaxial growth at the centers of

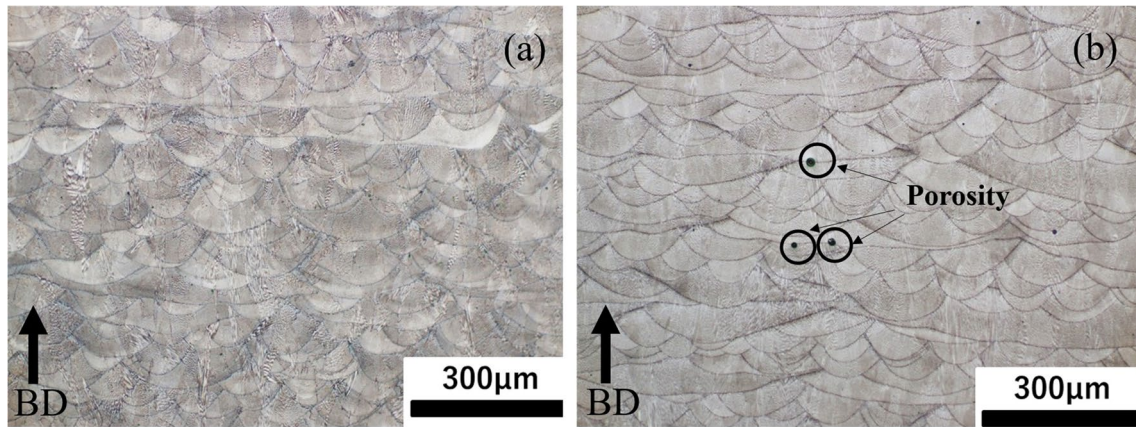


Fig. 6 Optical microstructures of molten pool boundary in the as-built (a) PH200 and (b) PH600 specimens

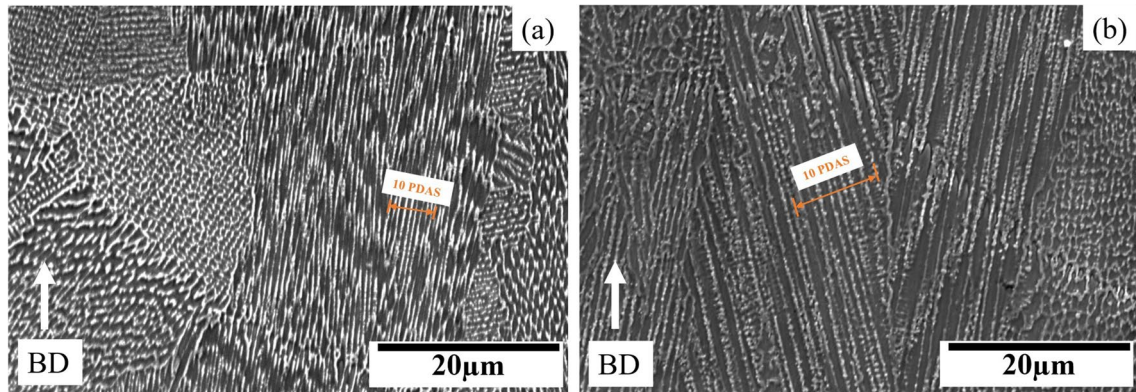

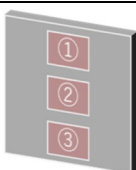
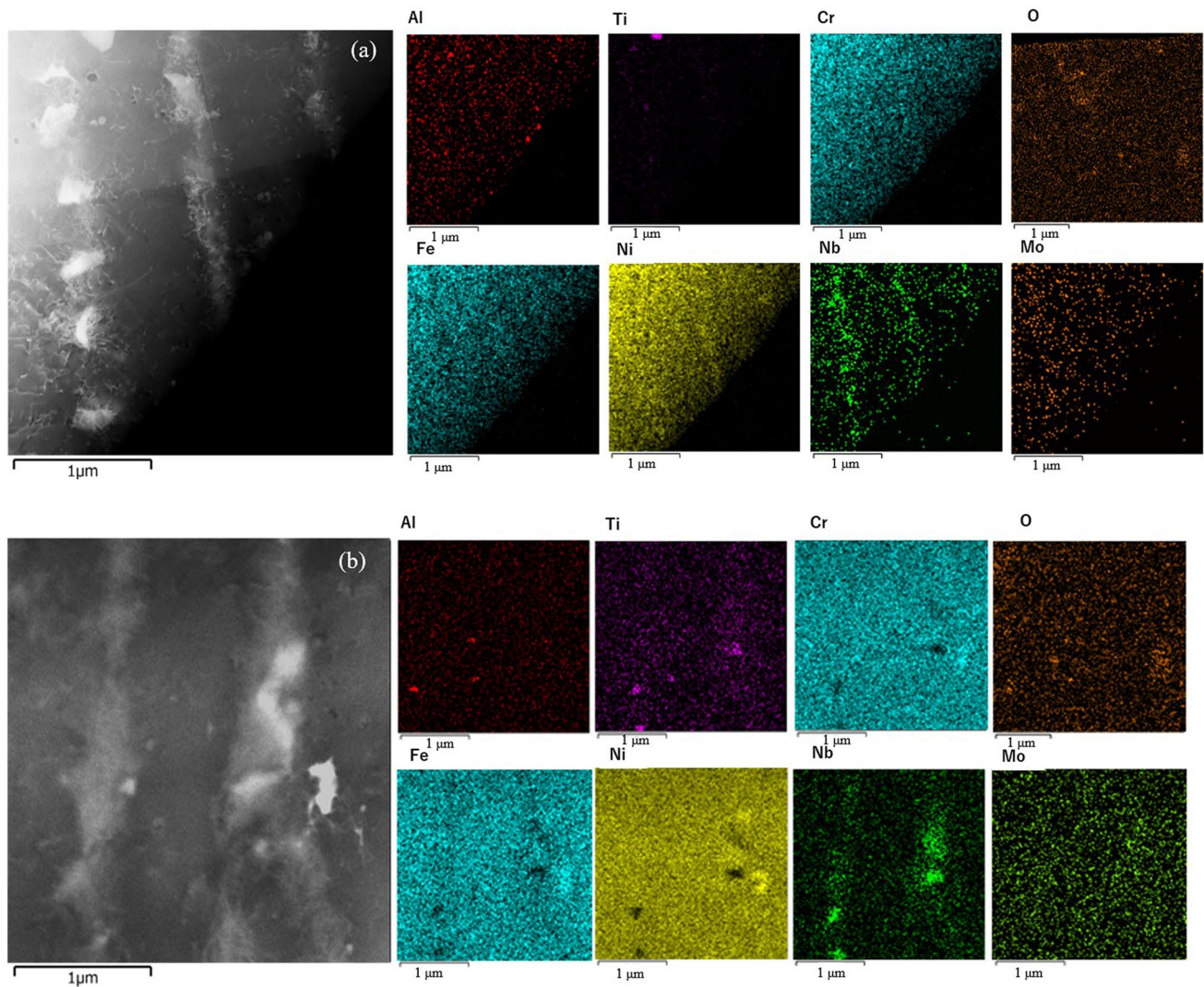


Fig. 7 SEM microstructures of the as-built (a, c) PH200 and (b, d) PH600 specimens

Table 5 Primary dendritic arm spacing ( $\lambda$ ) and cooling rate ( $\dot{T}$ ) of PH200 and PH600 as-built specimens

	PH200	Height* (mm)	Simulated Temperature (°C)	$\lambda$ ( $\mu\text{m}$ ) (avg. of 10 dendrites)	$\dot{T}$ (°C/sec)
	1	37.5	175.71	0.698	$8.98 \times 10^5$
	2	22.5	189.63	0.635	$1.16 \times 10^6$
	3	7.5	198.56	0.699	$8.94 \times 10^5$
	PH600	Height* (mm)	Simulated Temperature (°C)	$\lambda$ ( $\mu\text{m}$ ) (avg. of 10 dendrites)	$\dot{T}$ (°C/sec)
	1	37.5	534.61	1.085	$2.63 \times 10^5$
	2	22.5	572.31	0.963	$3.66 \times 10^5$
	3	7.5	596.19	0.953	$3.77 \times 10^5$

\* The height in Table 5 is taken from bottom to top



**Fig. 8** STEM-EDS microstructures show Nb segregation at the interdendritic regions of the as-built specimens of (a) PH200 and (b) PH600

molten pools, which resulted in a lower grain aspect ratio in the building direction (Fig. 10c). Almost all the grains in the PH600 specimen were oriented in the  $\langle 001 \rangle$  direction (red), and these are aligned parallel to the building direction. The PH200 specimen grains are a mixture of  $\langle 100 \rangle$  (red) and  $\langle 110 \rangle$  (green) orientation directions. The fine grains resulted from the material's complex heat history due to the overlap of laser scanning at the edges of the molten pools. Both the specimens' grains are oriented along the building direction.

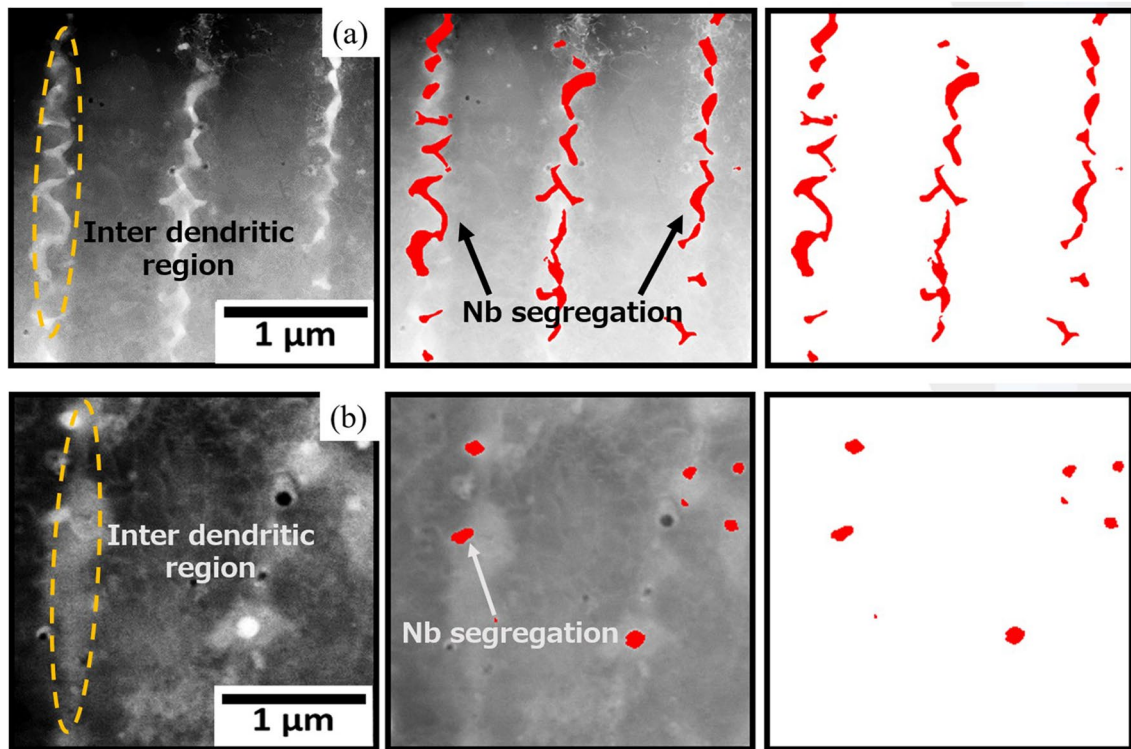
### 3.2.2 STA condition

Figure 11 presents the SEM microstructures of the heat-treated STA specimens. Molten pool boundaries were not observed in both specimens, and the microstructure was very fine in both. In the PH200 specimen (Fig. 11a) more Laves

and  $\delta$  phases were observed than in the PH600 specimen (Fig. 11b) at the interdendritic regions and grain boundaries. As the Laves phase mostly form  $\delta$  phase after heat treatment [41], slowing the cooling rate can reduce the  $\delta$  phases. However, a slower cooling rate of PH600 than PH200 (Table 5) leads to little  $\delta$  phase formation in PH600 (Fig. 11b).

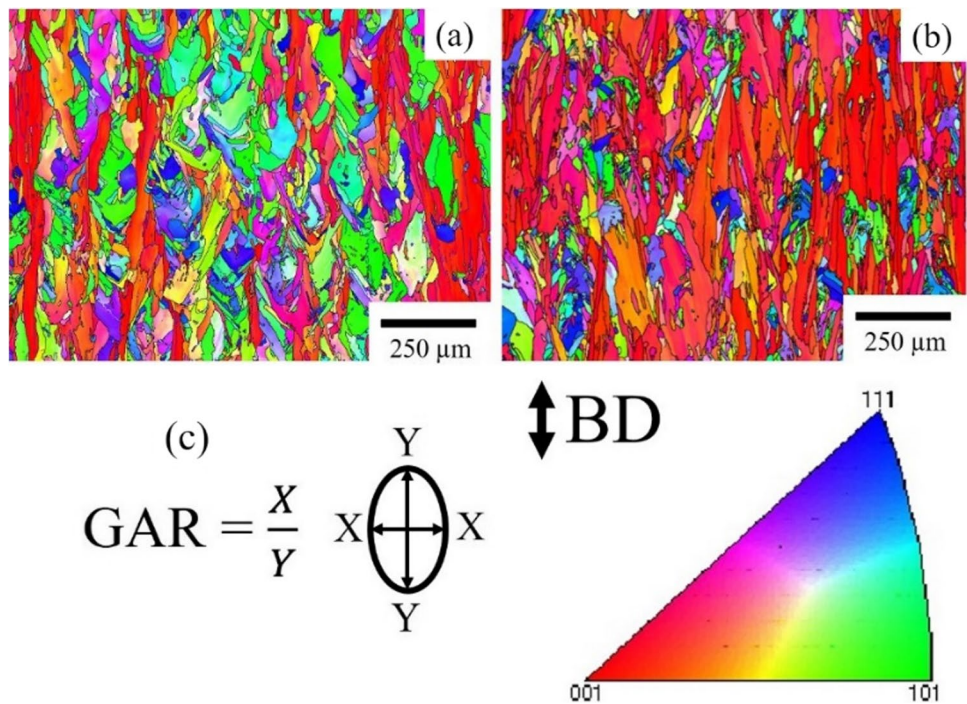
We calculated the  $\delta$ -phase size and volume fractions using ImageJ software, and the results are presented on the color maps and bar maps (Fig. 12). The differences between the PH200 and PH600 specimens were the size and volume fraction of the  $\delta$  phase. In the STA PH200 specimen, the  $\delta$  phase is needle-shaped (Fig. 12a), whereas, in the PH600 specimen, the  $\delta$  phase includes both round and needle-like shapes (Fig. 12b). The  $\delta$  phase evolved by consuming Nb, which was segregated during SLM and converted into a needle shape during the heat treatment. Figure 12c shows the volume fractions of the





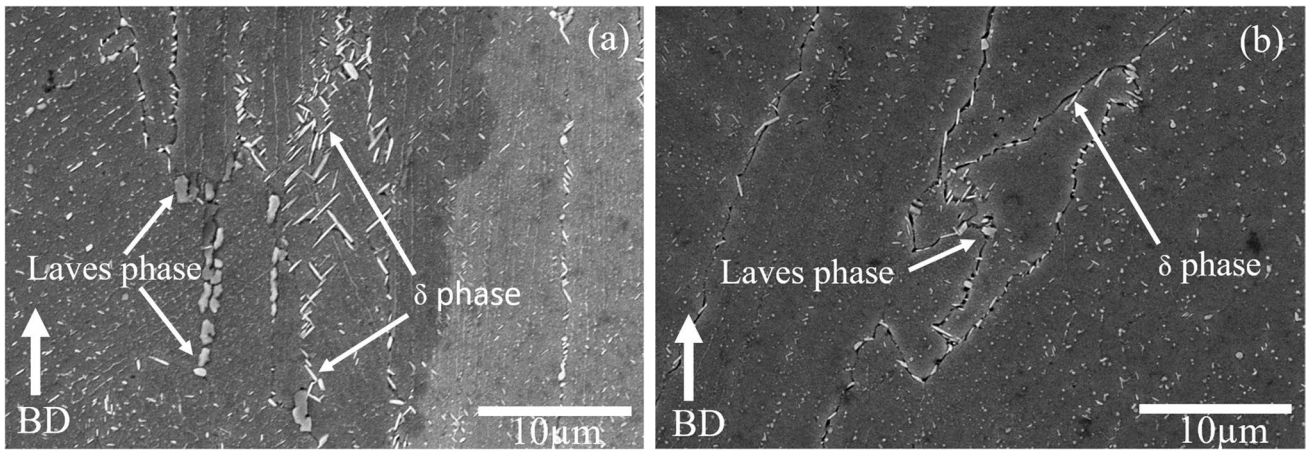
**Fig. 9** STEM microstructures of the Nb-rich area in as-built (a) PH200 and (b) PH600 specimens. The EDS map of Nb was binarized, and the Nb-rich area was obtained by ImageJ

**Fig. 10** Electron backscattered diffraction (EBSD) maps of the as-built (a) PH200 specimen and (b) PH600 specimen; (c) grain aspect ratio (GAR) and orientation map with indices



$\delta$  phase in the STA PH200 and PH600 specimens. While the PH600 specimen had a more minor  $\delta$  phase than the PH200 specimen, the  $\delta$  phase in the PH200 specimen was

much larger than that in the PH600 specimen. However, the PH600 specimen had far fewer  $\delta$  phases than that of the PH200 specimen.



**Fig. 11** SEM microstructures of the Laves phase and  $\delta$ -phase of the heat-treated (STA) specimens: (a) PH200 and (b) PH600

**Fig. 12**  $\delta$ -phase microstructures of the heat-treated (STA) specimens with ImageJ analysis color maps: (a) PH200 and (b) PH600; (c)  $\delta$ -phase size and area fraction bar graphs of PH200 and PH600 STA specimens

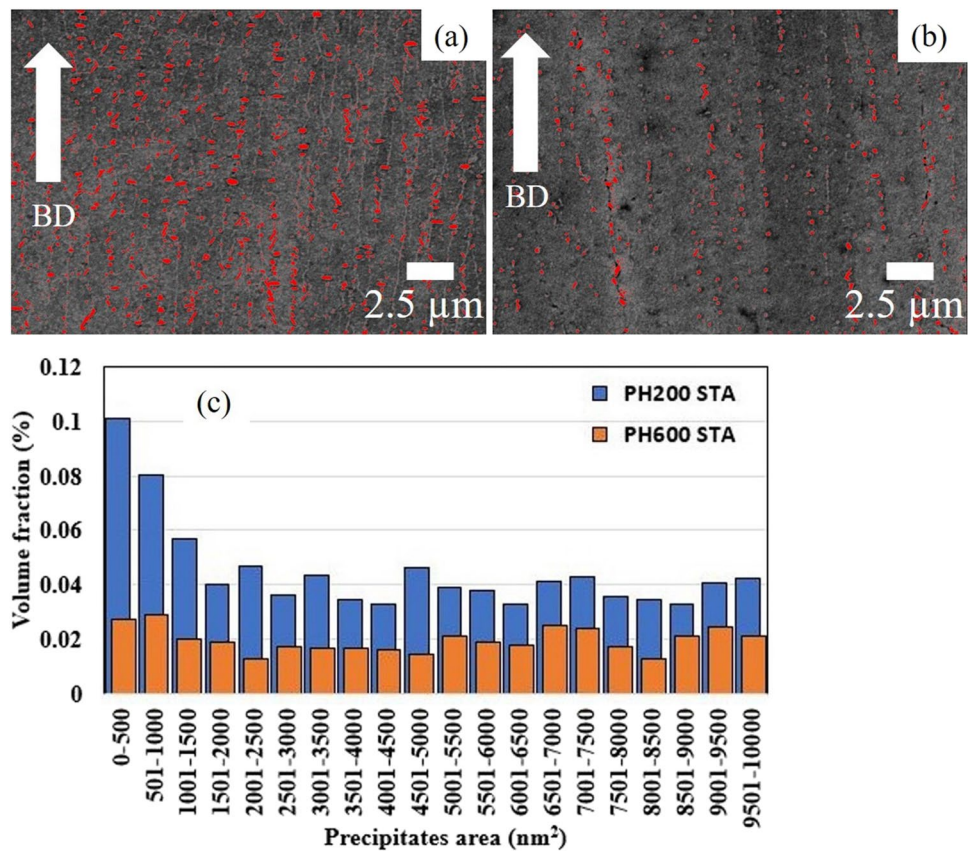
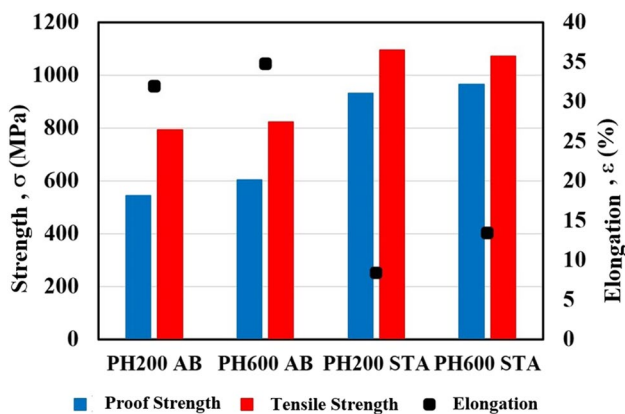
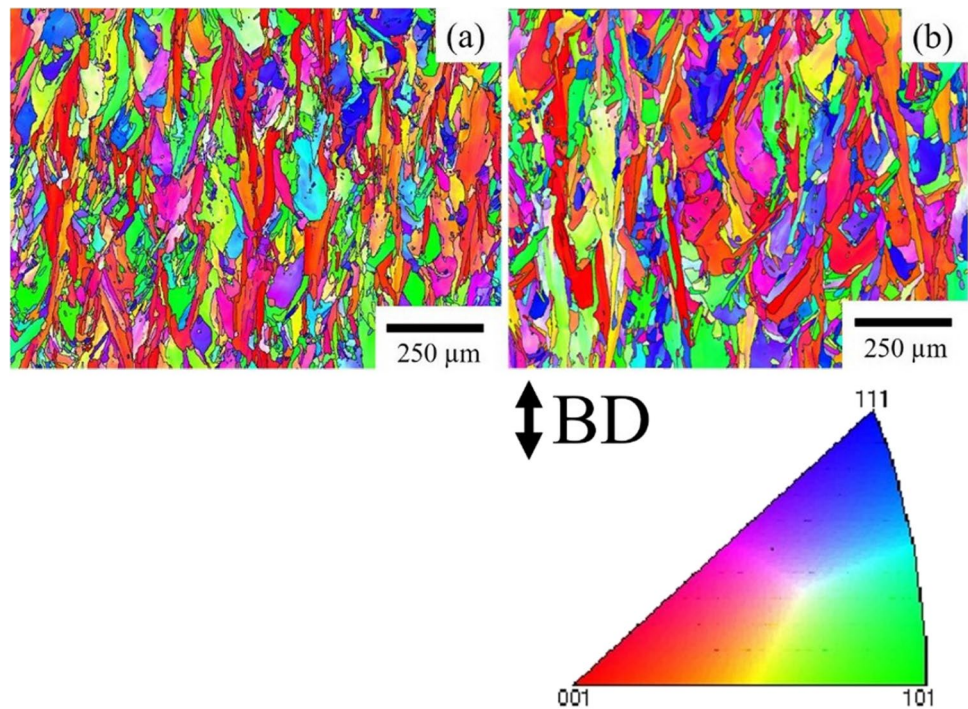


Figure 13 shows the EBSD maps and GARs of the STA specimens. The vertical direction is parallel to the building direction. The PH200 and PH600 specimens have similar microstructures as the as-built specimens, including columnar grains and fine grains (Fig. 13a, b respectively). Even after STA heat treatment, the columnar grains resulted in a lower grain aspect ratio in the building direction (Fig. 13c).

### 3.3 High-temperature mechanical properties

The tensile properties of the PH200 and PH600 specimens at high temperature (650°C) are shown in Fig. 14. In the as-built specimens, PH200 showed lower tensile properties than PH600. However the tensile elongation of the PH600 specimen differed significantly from that of the PH200 specimen. The tensile strengths were similar after the STA heat

**Fig. 13** Electron backscattered diffraction (EBSD) maps of the STA (a) PH200 and (b) PH600 specimens



**Fig. 14** Tensile properties at high temperature (650°C) of PH200 and PH600 specimens for the as-built and STA conditions

treatment, but tensile elongation was greater for the PH600 specimen.

Figure 15a presents the creep strain–time curves, and Fig. 15b illustrates the creep strain rate–time curves for the as-built and STA specimens under 650°C/550 MPa. The as-built PH200 specimen exhibited a creep life of 177 h, while the PH600 specimen exhibited a creep life 2.09 times higher, 370 h.

Moreover, PH600 showed a lower creep strain rate and a more significant rupture strain than PH200. After STA heat treatment, PH200’s creep life increased, and its creep strain rate vastly decreased compared to the as-built specimen. Whereas the STA PH600 creep life (993 h) was 2.17

times longer than that of PH200 (457 h), the creep strain rate was also reduced substantially. Figure 16 shows the rupture surfaces of the STA specimens after the creep test. As can be seen, both the PH200 and PH600 specimens showed brittle fractures due to fracturing along interdendritic regions.

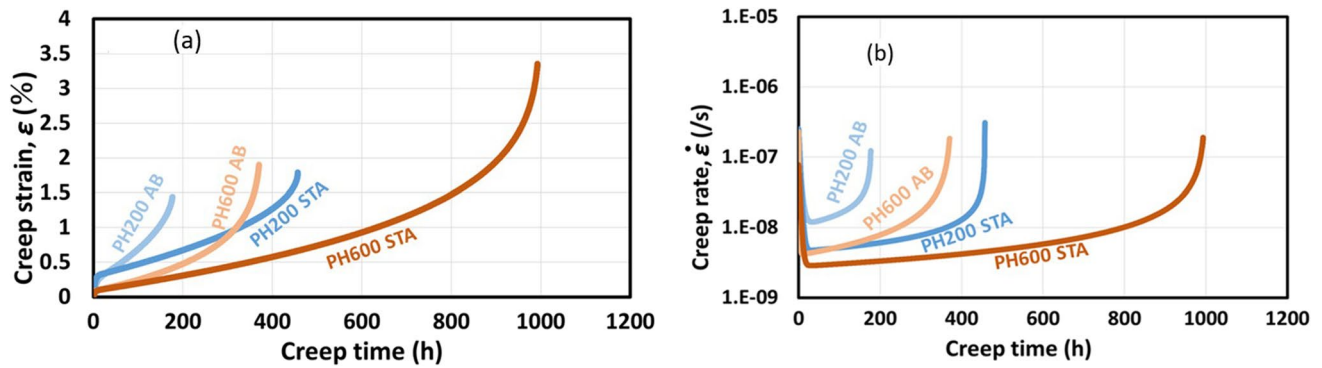
Figure 17 shows the microstructures of the STA specimens along the loading direction after the creep test. PH200 had large cracks (Fig. 17a) parallel to the δ-phase distribution (Fig. 17c). However, PH600 had a few large cracks along the interdendritic region (Fig. 17b, d).

Figure 18 shows the fracture surface from the high-temperature tensile test.

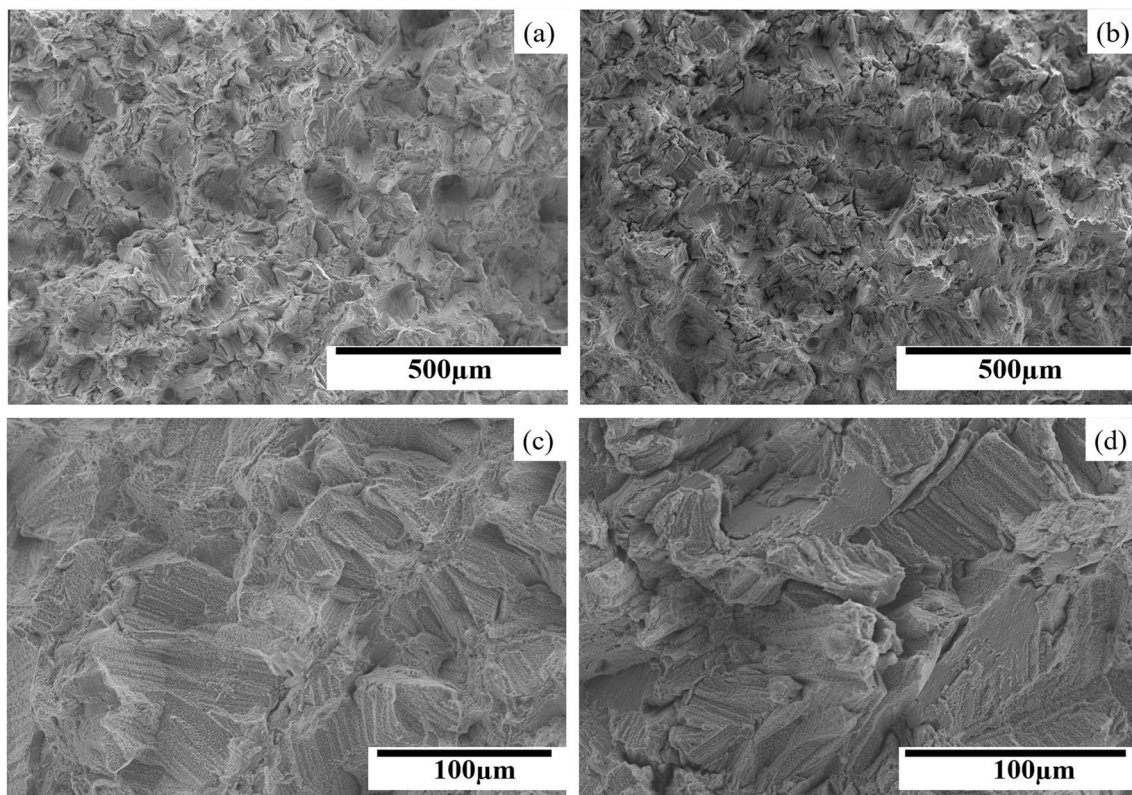
## 4 Discussion

### 4.1 Effect of base plate preheating on Nb segregation in the as-built specimens

The characteristics of Nb segregation in the as-built specimens differed between the PH200 and PH600 specimens. In PH200, more Nb segregation was observed uniformly along the interdendritic regions, and the spacing between Nb segregated areas was negligible (Fig. 8a, b). On the contrary, in PH600, Nb segregation was meager. ImageJ calculations showed that in the PH200 specimen, the Nb segregation area fractions were an average of 5.94% (Fig. 9a) and 0.84% in the PH600 as-built SLM specimen (Fig. 9b). The segregation of Nb at the interdendritic regions is due mainly to the base plate remaining at 200°C and 600°C in the PH200 and PH600 specimens,



**Fig. 15** Creep curves of as-built (AB) and STA specimens at 650°C/ 550 MPa: (a) creep strain vs. time curves and (b) creep strain rate vs. time curves



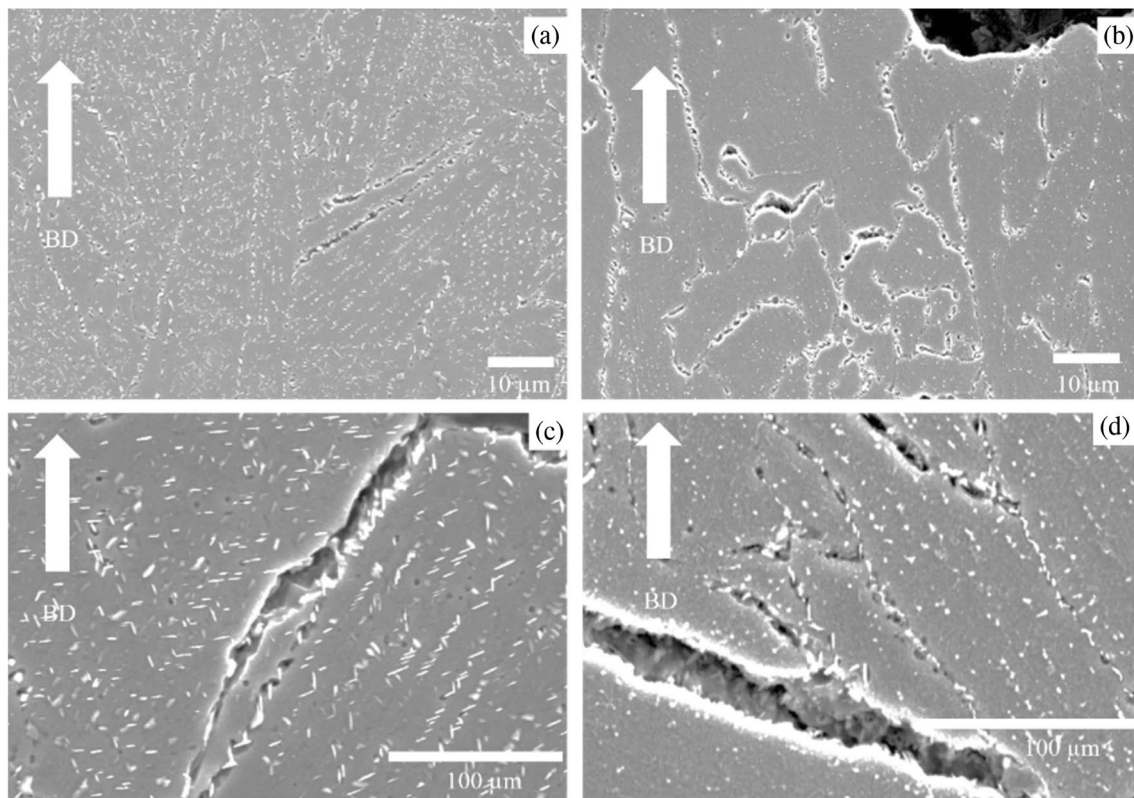
**Fig. 16** Creep-rupture surfaces of STA (a, c) PH200 and (b, d) PH600 specimens after creep rupture test at 650°C/ 550 MPa

respectively. This would cause the cooling rate difference between the specimens. In addition, the cooling rate during solidification is predicted by primary dendrite arm spacing ( $\lambda$ ).

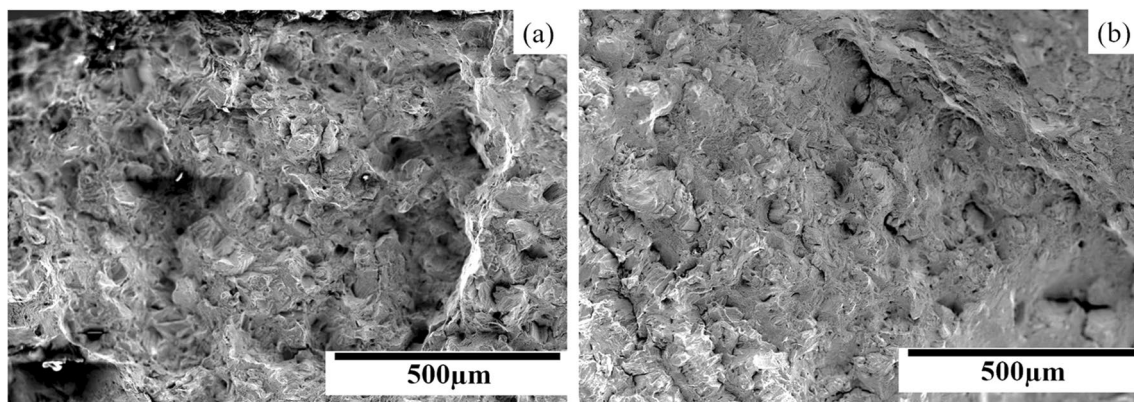
The relationship between primary dendrite arm spacing and the cooling rate is a linear function in a double logarithmic chart. Using a graph from the literature, the cooling rates of both specimens were calculated, as listed in Table 5 [50]. The cooling rates of the PH200 and PH600 as-built SLM specimens were calculated using Eq. 4, revealing a higher cooling rate in the PH200 specimen.

The simulation result showed that the preheated base plate transfers heat to the cube during the build process. Figure 5 illustrates the temperature along different positions of the cube in thermal equilibrium. The temperature difference between the top surface and the base plate is very little. So, preheated base plate influences the final model.

The PH600 specimen showed a dendritic structure, while the PH200 specimen showed a cellular network (Fig. 7a, b). By increasing the cooling rate, the transition from dendritic (preheated at 600°C) to cellular (preheated at 200°C) structures



**Fig. 17** Fracture microstructure on the side surface after creep rupture test of STA (a, c) PH200 and (b, d) PH600 specimens



**Fig. 18** Tensile fracture surface (a) PH200 and (b) PH600 specimens

[51] would occur. The dislocations formed within the cells and at cell boundaries are generated by the high stresses occurring during SLM [48]. The cellular structure results in higher dislocation density, leading to more pipe diffusion, which in turn causes the higher segregation of Nb along the interdendritic regions during solidification. This is suggested that the higher dislocation density near the cell boundaries than within the cells arises because the Nb-rich precipitates and the eutectic act as barriers to the glide of dislocations, which accumulate in these

regions with high precipitate density [45, 50]. In comparison, the cooling rate of the PH600 as-built specimen was reduced by holding the specimen at a higher temperature (600°C). This indicates that the dislocation density of the PH600 SLM specimen would be lower than that of the PH200 specimen.

The tensile strengths and elongation in the as-built PH600 specimen were higher than those of the PH200 specimen (Fig. 14). In addition, these microstructural differences affected creep properties between the as-built PH200 and

PH600 specimens. The as-built PH200 specimen exhibited lower creep life (177 h) and lower creep elongation (1.4%). The PH600 specimen showed longer creep life (370 h) than the PH200 specimen (Fig. 15a). The micro-segregation of Nb and other elements usually occurs in the conventional casting and welding of IN718. The segregated alloy elements in interdendritic regions could induce the precipitation of the Laves phase  $(\text{Ni, Cr, Fe})_2(\text{Nb, Mo, Ti})$ , resulting in the deterioration of the mechanical properties. The morphology of cellular dendrites and the chemical composition profiles across the cellular dendrites in the as-built SLM IN718 are shown in Fig. 8. The apparent segregation of Nb elements can also be directly observed between adjacent cellular dendrites in Fig. 9 [40]. The tensile and creep strengths would be increased because of the increase in the  $\gamma''$  volume fraction due to the decrease in the Laves volume fraction. The tensile and creep elongations would be increased because of the decreased volume fraction of the Laves phase and Nb carbide, thus increasing brittleness [45].

#### 4.2 Effect of $\delta$ -phase after STA heat treatment on mechanical properties

After the STA heat treatment, the microstructures of the PH200 and PH600 specimens were relatively different. The Laves phase observed in the as-built specimen transformed into the  $\delta$  phase. In the PH200 specimen, the  $\delta$  phase was formed by the consumption of a lot of Nb during heat treatment; many  $\delta$  phase precipitated uniformly along the interdendritic regions, and it is evident that the PH200 as-built specimen has a lot of segregation of Nb due to the higher cooling rate. Yttrium addition can make the needle-like  $\delta$  phase into globular  $\delta$  phase [52]. The presence of successive needle-shaped  $\delta$  precipitates, in conjunction with the poor coherency in STA specimens (Fig. 11a, b), resulted in low tensile properties in PH200 compared to the PH600 specimen (Fig. 14). In addition, the needle-shaped  $\delta$ -phase contributes to inferior creep life and poor elongation. That is, “ $\delta$ -phase embrittlement” would be the primary reason why the PH200 STA specimen showed a lower creep rupture life. This led to brittle fractures along the interdendritic regions due to crack initiation along with the  $\delta$  phase during the creep test. However, in the PH600 specimen, two different shapes of  $\delta$  phases, round and needle-shaped, were precipitated along the interdendritic region during heat treatment. Moreover, the  $\delta$  phases were precipitated discontinuously along with the interdendritic areas, and these are much lower fractions than those of the PH200 STA specimen. This contributed to higher tensile elongation in the PH600 specimen than in the PH200. Despite that, the PH600 specimen experienced brittle fractures along the interdendritic region during the creep test. Although there were some voids and micro-cracks, it was difficult for the cracks to propagate due to the lack of  $\delta$  phases and their discontinuous distribution.

Thus, the PH600 specimen exhibited a longer creep life than the PH200 specimen. In addition, the creep properties of the PH200 and PH600 specimens were higher than those of the IN718 STA specimen built without preheating, which showed a cellular structure and poor creep-rupture life of 134 h, as well as poor creep-rupture elongation [53]. This evidence indicates that preheating is effective in improving creep properties. Moreover, the PH600 specimen creep life was nearly comparable to that of a C&W specimen (*creep life* = 1230 h, *elongation* = 8.1%) [53]. Micro cracks along the  $\delta$  phase would be formed on the  $\{111\}$  planes in creep-ruptured STA specimens without preheating [53]. Fracturing along the dendritic structure was also observed in the specimen as shown in (Fig. 17c, d). In the STA specimen, the successive  $\delta$  precipitates would provide the initiation sites of crack during the creep test. As a result, cracks would easily propagate along the successive  $\delta$  precipitates and bring about an inferior creep life. Nevertheless, it was still lower than C&W, mainly because the  $\delta$  phase precipitates are concentrated in the interdendritic region in the PH600 AM specimen due to Nb segregation. In contrast, they form uniformly within the grain in wrought material [54]. As mentioned, when the cooling rate was increased, the transition from dendritic (preheated at 600°C) to cellular (preheated at 200°C) structures was observed. The dislocations formed within the cells and at cell boundaries are generated by the high stresses occurring during SLM, which in the case of CM247LC leads to extensive cracking [48]. In the case of CM247LC, the higher dislocation density near the cell boundaries than within the cells arises because the Hf/W/Ti/Ta-rich precipitates and the eutectic act as barriers to the glide of dislocations, which therefore accumulate in these regions of high precipitate density. In IN718, the  $\delta$  phase and carbide precipitates would make a barrier to dislocation motion.

Thus, the effects of base plate preheating in SLM on the mechanical properties of IN718 superalloy brought about the microstructural change from a cellular to a dendritic structure. They improved the mechanical properties by decreasing the cooling rate.

## 5 Conclusions

This study investigated the effects of base plate preheating on the mechanical properties of selective laser melted (SLM) IN718 superalloy. The key findings are:

- A) The temperature distributions and microstructure in the blocks were found to be relatively uniform during the building process because both the built block and surrounding power are preheated.
- B) The PH200 as-built specimen showed a cellular structure and greater Nb segregation at the interdendritic region

than the PH600 specimen (dendritic structure). This is due to the cooling rate differences for the two different temperature preheated base plate.

- C) The STA heat-treated PH200 specimen experienced brittle fractures due to the formation of more needle-like  $\delta$ -phases, causing rapid crack propagation, in turn resulting in inferior creep life, creep rupture, and tensile elongation compared to the PH600 specimen. The STA heat-treated PH600 specimen had a small number of  $\delta$  phases resulted in better creep life, creep rate, and tensile elongation.
- D) The PH600 specimen showed higher strength properties than the PH200 specimens due to its more significant volume fraction of  $\gamma''$  phase in the  $\gamma$ -matrix (which is the primary strengthening phase in IN718 superalloy), by reducing Nb-rich phases (Laves and  $\delta$  phases) in the interdendritic region.

**Acknowledgements** This work was supported by the Japan Society for the Promotion of Science (Grants-in-Aid for Scientific Research) (JSPS KAKENHI) (Grant Number 22H01366).

**Author contributions** All authors contributed to the study conception and design. The material preparation was done by Shohei Ishisako. Experimental tests, data collection, and analysis were performed by Yusuke Shinoda, Palleda Thaviti Naidu. The simulation was done by Hasina Tabassum Chowdhury and Naoto Kakuta. The first draft of the manuscript was written by Koji Kakehi, Yusuke Shinoda, and Hasina Tabassum Chowdhury and review was done by Naoto Kakuta. All authors read and approved the final manuscript.

**Funding** Open access funding provided by Tokyo Metropolitan University.

## Declarations

**Competing interests** The authors have no relevant financial or non-financial interests to disclose.

**Open Access** This article is licensed under a Creative Commons Attribution 4.0 International License, which permits use, sharing, adaptation, distribution and reproduction in any medium or format, as long as you give appropriate credit to the original author(s) and the source, provide a link to the Creative Commons licence, and indicate if changes were made. The images or other third party material in this article are included in the article's Creative Commons licence, unless indicated otherwise in a credit line to the material. If material is not included in the article's Creative Commons licence and your intended use is not permitted by statutory regulation or exceeds the permitted use, you will need to obtain permission directly from the copyright holder. To view a copy of this licence, visit <http://creativecommons.org/licenses/by/4.0/>.

## References

- Wong KV, Hernandez A (2012) A review of additive manufacturing. *Int Sch Res Not* 2012:e208760. <https://doi.org/10.5402/2012/208760>
- Uhlmann E, Kersting R, Klein TB, Cruz MF, Borille AV (2015) Additive manufacturing of titanium alloy for aircraft components. *Procedia CIRP* 35:55–60. <https://doi.org/10.1016/j.procir.2015.08.061>
- Olakanmi EO, Cochrane RF, Dalgarno KW (2015) A review on selective laser sintering/melting (SLS/SLM) of aluminium alloy powders: processing, microstructure, and properties. *Prog Mater Sci* 74:401–477. <https://doi.org/10.1016/j.pmatsci.2015.03.002>
- Suryawanshi J, Prashanth KG, Ramamurty U (2017) Mechanical behavior of selective laser melted 316L stainless steel. *Mater Sci Eng A* 696:113–121. <https://doi.org/10.1016/j.msea.2017.04.058>
- Frazier WE (2014) Metal additive manufacturing: a review. *J Mater Eng Perform* 23(6):1917–1928. <https://doi.org/10.1007/s11665-014-0958-z>
- Herzog D, Seyda V, Wycisk E, Emmelmann C (2016) Additive manufacturing of metals. *Acta Mater* 117:371–392. <https://doi.org/10.1016/j.actamat.2016.07.019>
- Chen L, He Y, Yang Y, Niu S, Ren H (2017) The research status and development trend of additive manufacturing technology. *Int J Adv Manuf Technol* 89(9):3651–3660. <https://doi.org/10.1007/s00170-016-9335-4>
- Gibson I, Rosen D, Stucker B (2015) Additive manufacturing technologies: 3D printing, rapid prototyping, and direct digital manufacturing. Springer, New York. <https://doi.org/10.1007/978-1-4939-2113-3>
- Wang Z, Palmer TA, Beese AM (2016) Effect of processing parameters on microstructure and tensile properties of austenitic stainless steel 304L made by directed energy deposition additive manufacturing. *Acta Mater* 110:226–235. <https://doi.org/10.1016/j.actamat.2016.03.019>
- Wang P, Li HC, Prashanth KG, Eckert J, Scudino S (2017) Selective laser melting of Al-Zn-Mg-Cu: heat treatment, microstructure and mechanical properties. *J Alloys Compd* 707:287–290. <https://doi.org/10.1016/j.jallcom.2016.11.210>
- Rafi HK, Karthik NV, Gong H, Starr TL, Stucker BE (2013) Microstructures and mechanical properties of Ti6Al4V parts fabricated by selective laser melting and electron beam melting. *J Mater Eng Perform* 22(12):3872–3883. <https://doi.org/10.1007/s11665-013-0658-0>
- Prashanth KG, Eckert J (2017) Formation of metastable cellular microstructures in selective laser melted alloys. *J Alloys Compd* 707:27–34. <https://doi.org/10.1016/j.jallcom.2016.12.209>
- Banoth S, Palleda TN, Saito T, Murakami H, Kakehi K (2022) Effects of yttrium and silicon contents in Hastelloy-X built by selective laser melting process. *J Alloys Compd* 896:163050. <https://doi.org/10.1016/j.jallcom.2021.163050>
- Deng D (2018) Additively manufactured Inconel 718: microstructures and mechanical properties. Linköping University, Linköping University Electronic Press. Accessed 22 Jun 2023. [Online]. <https://doi.org/10.3384/lic.diva-144491>
- Plotkowski A, Kirka MM, Babu SS (2017) Verification and validation of a rapid heat transfer calculation methodology for transient melt pool solidification conditions in powder bed metal additive manufacturing. *Addit Manuf* 18:256–268. <https://doi.org/10.1016/j.addma.2017.10.017>
- Zhang D, Feng Z, Wang C, Wang W, Liu Z, Niu W (2018) Comparison of microstructures and mechanical properties of Inconel 718 alloy processed by selective laser melting and casting. *Mater Sci Eng A* 724:357–367. <https://doi.org/10.1016/j.msea.2018.03.073>
- Ströbner J, Terock M, Glatzel U (2015) Mechanical and microstructural investigation of nickel-based superalloy IN718 manufactured by selective laser melting (SLM). *Adv Eng Mater* 17(8):1099–1105. <https://doi.org/10.1002/adem.201500158>
- Hadadzadeh A, Baxter C, Amirkhiz BS, Mohammadi M (2018) Strengthening mechanisms in direct metal laser sintered AlSi10Mg: comparison between virgin and recycled powders. *Addit Manuf* 23:108–120. <https://doi.org/10.1016/j.addma.2018.07.014>
- Asgari H, Baxter C, Hosseinkhani K, Mohammadi M (2017) On microstructure and mechanical properties of additively manufactured AlSi10Mg\_200C using recycled powder. *Mater Sci Eng A* 707:148–158. <https://doi.org/10.1016/j.msea.2017.09.041>

20. Renderos M, Torregaray A, Gutierrez-Orrantia ME, Lamikiz A, Saintier N, Girof F (2017) Microstructure characterization of recycled IN718 powder and resulting laser clad material. *Mater Charact* 134:103–113. <https://doi.org/10.1016/j.matchar.2017.09.029>
21. Banoth S, Palleda TN, Shimazu S, Kakehi K (2021) Yttrium's effect on the hot cracking and creep properties of a Ni-based superalloy built up by additive manufacturing. *Materials* 14(5):Art. no. 5. <https://doi.org/10.3390/ma14051143>
22. Wan HY, Zhou ZJ, Li CP, Chen GF, Zhang GP (2019) Effect of scanning strategy on mechanical properties of selective laser melted Inconel 718. *Mater Sci Eng A* 753:42–48. <https://doi.org/10.1016/j.msea.2019.03.007>
23. Zhang B, Liao H, Coddet C (2012) Effects of processing parameters on properties of selective laser melting Mg–9%Al powder mixture. *Mater Des* 34:753–758. <https://doi.org/10.1016/j.matdes.2011.06.061>
24. Cherry JA, Davies HM, Mehmood S, Lavery NP, Brown SGR, Siens J (2015) Investigation into the effect of process parameters on microstructural and physical properties of 316L stainless steel parts by selective laser melting. *Int J Adv Manuf Technol* 76(5):869–879. <https://doi.org/10.1007/s00170-014-6297-2>
25. Zhao Z, Li L, Yang W, Zeng Y, Lian Y, Yue Z (2022) A comprehensive study of the anisotropic tensile properties of laser additive manufactured Ni-based superalloy after heat treatment. *Int J Plast* 148:103147. <https://doi.org/10.1016/j.ijplas.2021.103147>
26. Lu Y et al (2015) Study on the microstructure, mechanical property and residual stress of SLM Inconel-718 alloy manufactured by differing island scanning strategy. *Opt Laser Technol* 75:197–206. <https://doi.org/10.1016/j.optlastec.2015.07.009>
27. Pu H et al (2023) Thermo-mechanical analysis of Ti-6Al-4V Taylor bar using advanced joint path strategies based on additive manufacturing. *CIRP J Manuf Sci Technol* 40:167–179. <https://doi.org/10.1016/j.cirpj.2022.11.009>
28. Bai R et al (2023) Influence of the advanced joint path strategies on the energy absorption capacity of Ti-6Al-4V Taylor bar based on additive manufacturing. *J Therm Stress* 46(2):140–162. <https://doi.org/10.1080/01495739.2022.2149646>
29. Xing S et al (2023) Improved evolutionary structural optimization for Taylor bar impact problem based on additive manufacturing technique. In: 2023 International Conference on Advanced Robotics and Mechatronics (ICARM). pp 464–468. <https://doi.org/10.1109/ICARM58088.2023.10218761>
30. Cheng Y, Xiao Z, Zhu H, Zeng X, Wang G (2019) Influence of substrate characteristics on residual stress of SLMed Inconel 718. *Rapid Prototyp J* 25(4):792–799. <https://doi.org/10.1108/RPJ-09-2018-0238>
31. Jia Q, Gu D (2014) Selective laser melting additive manufacturing of Inconel 718 superalloy parts: densification, microstructure and properties. *J Alloys Compd* 585:713–721. <https://doi.org/10.1016/j.jallcom.2013.09.171>
32. Furrer D, Fecht H (1999) Ni-based superalloys for turbine discs. *JOM* 51(1):14–17. <https://doi.org/10.1007/s11837-999-0005-y>
33. Pollock TM, Tin S (2006) Nickel-based superalloys for advanced turbine engines: chemistry, microstructure and properties. *J Propuls Power* 22(2):361–374. <https://doi.org/10.2514/1.18239>
34. Guandalini G, Campanari S, Romano MC (2015) Power-to-gas plants and gas turbines for improved wind energy dispatchability: energy and economic assessment. *Appl Energy* 147:117–130. <https://doi.org/10.1016/j.apenergy.2015.02.055>
35. Warren J, Wei DY (2006) The cyclic fatigue behavior of direct age 718 at 149, 315, 454 and 538°C. *Mater Sci Eng A* 428(1):106–115. <https://doi.org/10.1016/j.msea.2006.04.091>
36. Zhang D, Niu W, Cao X, Liu Z (2015) Effect of standard heat treatment on the microstructure and mechanical properties of selective laser melting manufactured Inconel 718 superalloy. *Mater Sci Eng A* 644:32–40. <https://doi.org/10.1016/j.msea.2015.06.021>
37. Jia Q, Gu D (2014) Selective laser melting additive manufactured Inconel 718 superalloy parts: high-temperature oxidation property and its mechanisms. *Opt Laser Technol* 62:161–171. <https://doi.org/10.1016/j.optlastec.2014.03.008>
38. Brenne F, Niendorf T, Maier HJ (2013) Additively manufactured cellular structures: impact of microstructure and local strains on the monotonic and cyclic behavior under uniaxial and bending load. *J Mater Process Technol* 213(9):1558–1564. <https://doi.org/10.1016/j.jmatprotec.2013.03.013>
39. Banoth S, Li C-W, Hiratsuka Y, Kakehi K (2020) The effect of recrystallization on creep properties of alloy IN939 fabricated by selective laser melting process. *Metals* 10(8):Art. no. 8. <https://doi.org/10.3390/met10081016>
40. Tao P, Li H, Huang B, Hu Q, Gong S, Xu Q (2019) The crystal growth, intercellular spacing and microsegregation of selective laser melted Inconel 718 superalloy. *Vacuum* 159:382–390. <https://doi.org/10.1016/j.vacuum.2018.10.074>
41. Kakehi K, Banoth S, Kuo Y-L, Hayashi S (2020) Effect of yttrium addition on creep properties of a Ni-base superalloy built up by selective laser melting. *Scr Mater* 183:71–74. <https://doi.org/10.1016/j.scriptamat.2020.03.014>
42. Doubenskaia M, Domashenkov A, Smurov I, Petrovskiy P (2018) Study of selective laser melting of intermetallic TiAl powder using integral analysis. *Int J Mach Tools Manuf* 129:1–14. <https://doi.org/10.1016/j.ijmachtools.2018.02.003>
43. Park J-H et al (2022) Effect of preheating temperature on microstructural and mechanical properties of Inconel 718 fabricated by selective laser melting. *Met Mater Int* 28(11):2836–2848. <https://doi.org/10.1007/s12540-022-01169-w>
44. Chen Q et al (2021) Elucidating the effect of preheating temperature on melt pool morphology variation in Inconel 718 laser powder bed fusion via simulation and experiment. *Addit Manuf* 37:101642. <https://doi.org/10.1016/j.addma.2020.101642>
45. Kuo Y-L, Kakehi K (2017) Influence of powder surface contamination in the Ni-based superalloy alloy718 fabricated by selective laser melting and hot isostatic pressing. *Metals* 7(9):Art. no. 9. <https://doi.org/10.3390/met7090367>
46. Mills KC (2002) Ni - IN 718. In: Mills KC (ed) Recommended values of thermophysical properties for selected commercial alloys. Woodhead Publishing Series in Metals and Surface Engineering, Woodhead Publishing, pp 181–190. <https://doi.org/10.1533/9781845690144.181>
47. Willy HJ et al (2018) Model of laser energy absorption adjusted to optical measurements with effective use in finite element simulation of selective laser melting. *Mater Des* 157:24–34. <https://doi.org/10.1016/j.matdes.2018.07.029>
48. Wang X, Carter LN, Pang B, Attallah MM, Loretto MH (2017) Microstructure and yield strength of SLM-fabricated CM247LC Ni-superalloy. *Acta Mater* 128:87–95. <https://doi.org/10.1016/j.actamat.2017.02.007>
49. Guraya T, Singamneni S, Chen ZW (2019) Microstructure formed during selective laser melting of IN738LC in keyhole mode. *J Alloys Compd* 792:151–160. <https://doi.org/10.1016/j.jallcom.2019.03.419>
50. Nagahari T, Nagoya T, Kakehi K, Sato N, Nakano S (2020) Microstructure and creep properties of Ni-base superalloy IN718 built up by selective laser melting in a vacuum environment. *Metals* 10(3):Art. no. 3. <https://doi.org/10.3390/met10030362>
51. Yin H, Felicelli SD (2010) Dendrite growth simulation during solidification in the LENS process. *Acta Mater* 58(4):1455–1465. <https://doi.org/10.1016/j.actamat.2009.10.053>
52. Naidu Palleda T, Banoth S, Tanaka M, Murakami H, Kakehi K (2023) The role of yttrium micro-alloying on microstructure evolution and high-temperature mechanical properties of additively manufactured Inconel 718. *Mater Des* 225:111567. <https://doi.org/10.1016/j.matdes.2022.111567>
53. Kuo Y-L, Horikawa S, Kakehi K (2017) Effects of build direction and heat treatment on creep properties of Ni-base superalloy built



- up by additive manufacturing. *Scr Mater* 129:74–78. <https://doi.org/10.1016/j.scriptamat.2016.10.035>
54. Idell Y et al (2016) Unexpected  $\delta$ -phase formation in additive-manufactured Ni-based superalloy. *JOM* 68(3):950–959. <https://doi.org/10.1007/s11837-015-1772-2>

**Publisher's Note** Springer Nature remains neutral with regard to jurisdictional claims in published maps and institutional affiliations.